

# Porous, Multi-layered Piezoelectric Composites Based on Highly Oriented Pzt/pvdf Electrospinning Fibers for High-performance Piezoelectric Nanogenerators

**Xiangxin Du**

Zhejiang University School of Materials Science and Engineering

**Zheng Zhou**

Zhejiang University School of Materials Science and Engineering

**Zhao Zhang**

Zhejiang University School of Materials Science and Engineering

**Liqin Yao**

Zhejiang University School of Materials Science and Engineering

**Qilong Zhang** (✉ [mse237@zju.edu.cn](mailto:mse237@zju.edu.cn))

Zhejiang University

**Hui Yang**

Zhejiang University School of Materials Science and Engineering

---

## Research Article

**Keywords:** Piezoelectric composite, Piezoelectric nanogenerator, Porous structure, PZT/PVDF electrospinning fibers, Flexible self-powered devices

**Posted Date:** May 13th, 2021

**DOI:** <https://doi.org/10.21203/rs.3.rs-505664/v1>

**License:**  This work is licensed under a Creative Commons Attribution 4.0 International License.

[Read Full License](#)

---

**Version of Record:** A version of this preprint was published at Journal of Advanced Ceramics on January 11th, 2022. See the published version at <https://doi.org/10.1007/s40145-021-0537-3>.

# Abstract

Piezoelectric nanogenerators (PENGs) that can harvest mechanical energy from ambient environment have broad prospects for multi-functional applications. Here, multi-layered piezoelectric composites with a porous structure based on highly oriented PZT/PVDF electrospinning fibers are prepared via a laminating method to construct high-performance PENGs. PZT particles as piezoelectric reinforcing phases are embedded in PVDF fibers and facilitate the formation of polar  $\beta$  phase in PVDF. The multi-layered, porous structure effectively promotes the overall polarization and surface bound charge density, resulting in highly efficient electromechanical conversion. The PENG based on 10 wt.% PZT/PVDF composite fibers with a 220  $\mu\text{m}$  film thickness output an optimal voltage of 62.0 V and a power of 136.9  $\mu\text{W}$ , which is 3.4 and 6.5 times the voltage and power of 10wt.% PZT/PVDF casting film-based PENG, respectively. Importantly, the PENG shows a high sensitivity of  $12.4 \text{ VN}^{-1}$ , presenting a significant advantage in comparison to PENGs with other porous structures. In addition, the composites show excellent flexibility with a Young's modulus of 227.2 MPa and an elongation of 262.3%. This work shows great potential application of piezoelectric fiber composites in flexible energy harvesting devices.

## Introduction

With the urgent need for multifunctional, portable, light and wearable electronic devices, piezoelectric nanogenerators (PENGs) capable of high-efficiency energy harvesting from ambient environment are used as self-powered devices nowadays. PENG converts the stress applied on the material into electricity by means of the inherent piezoelectric effect. Piezoelectric effect refers to the phenomenon in which the material without a center of structural symmetry changes its internal polarization with external pressure, giving rise to the same amount of heterogeneous charges on the surface. At first, perovskite piezoelectric ceramics ((K,Na,Li)NbO<sub>3</sub>[1,2], BaTiO<sub>3</sub>[3] and Pb(Zr,Ti)O<sub>3</sub>[4,5] and piezoelectric semiconductors (ZnS[6], ZnO[7] and CdS[8]) attracted lots of attention due to their excellent piezoelectric coefficients, but the brittleness of their own limits the application in flexible electric devices. On the contrary, piezoelectric polymer has good flexibility but much lower piezoelectric coefficient comparing to the piezoceramics/semiconductors. Therefore, a large number of organic/inorganic composites-based PENGs with complementary advantages of piezoelectric ceramics/semiconductors and polymers have become the focus of academic research.

To date, the familiar structure of the piezoelectric composites is to embed piezoelectric inorganic particles simply and randomly into flexible polymers[9]. This structure integrates the advantages of piezoelectric ceramics/semiconductors and polymers, but not effectively better the output performance of the composite-based PENGs because of particle aggregation[10] or isolation microstructure[11], as well as insufficient flexibility. Hence, some other novel structures are proposed to solve the problems. For instance, vertically aligned BaTiO<sub>3</sub> nanowires-based PENGs[12] are developed to reduce the isolation microstructure, getting an output power of  $6.27 \text{ mWcm}^{-2}$ . A three-dimensional porous network structure[13] is reported to ensure the dispersion uniformity of piezoelectric particles in the matrix. In

addition, stress transfer is also enhanced, which is further simulated by Comsol simulation[14], demonstrating an effective load transfer.

It is obvious that porous structure plays an important role for PENGs to improve flexibility, load transfer and uniformity of particle dispersion. Another porous structure based on fibers possesses the most satisfactory mechanical features such as light, flexible, and stretchable, which makes the material ideal to be applied as the interface platform among humans, environment, and machines[15,16]. Electrospinning is a mature and applicable technique for generating ultrathin fibers to be used in various field like biomedical science, filtration, energy harvesting, etc[17,18]. Considering the PENGs for energy harvesting, most fiber-based PENGs are made of membranes originally from electrospinning. For example, the BCTZ–0.2mol% Y nanofibers are fabricated through electrospinning technology[19], and a voltage of 3V is generated by finger tapping. (Na,K)NbO<sub>3</sub>-based P(VDF-TrFE) electrospinning nanofibers are also reported, the corresponding open-circuit voltage reaches 12.2V, and the highest power is 33.2μW[20]. Additionally, PZT/PVDF composite fibers combining the strengths of the excellent piezoelectricity and flexibility are studied. Some[21,22] focus on the piezoelectric performance of original electrospinning fibers, whose output voltage is as small as 184 mV. Others[23,24] study the ferroelectric, dielectric and mechanical properties of the PZT/PVDF fiber film, but do not give a description of output performance. It can be concluded that the output power of the membranes directly obtained by electrospinning is still low. To be specific, in the process of electrospinning, the low conductivity of polymer fibers causes residual charges to accumulate on the surface of collected fibers[25], which hinders further fibers collecting from the similarly charged jet. As a result, the adhesion between the fibers is reduced and a loose structure is formed. The largely loose structure leads to poor membrane resilience and low fiber density, limiting the output power of the membrane. Besides, it is difficult for the membranes to be sandwiched directly into electrodes without destroying fiber arrangement.

In this work, we have successfully prepared the dense fiber films with a multi-layered porous structure consisting of contact surface fibers and separated internal fibers via a laminating method, where PVDF as a flexible piezoelectric substrate was dissolved to be electro spun into oriented fibers due to the advantages of high flexibility, good piezoelectricity and low cost[26]. In addition, PZT particles with excellent piezoelectricity and large residual polarization were imbedded into the fibers to further enhance the piezoelectric capability. Herein, we explored the structural characteristics and the piezoelectric output performance of the PENGs based on the PZT/PVDF flexible piezoelectric composite with a multi-layered, porous fibrous structure. Differing from conventional piezoelectric composites, the PZT/PVDF fiber composites with multi-layered, porous fibrous structure exhibit superior electrical properties. The 10wt.% PZT/PVDF composite fiber-based PENG (220μm) output the maximum voltage of 62.0 V and the power of 136.9 μW, which are 3.4 times and 6.5 times that of the control PENG (10wt.% PZT/PVDF casting film-based PENG under a periodic pressure of 5N. This work provides an efficient but simple way to prepare high-performance small-scale PENGs.

# Experimental Procedures

## 2.1 Preparation of precursor solution

The  $\text{Pb}(\text{Zr}_{0.52}\text{Ti}_{0.48})\text{O}_3$  (PZT) powders were prepared by means of the high-energy ball milling method[27]. The precursor solution shown in Fig. 1(a) was prepared as follows: First, a certain amount of PZT powders were ultrasonically dispersed in a mixture of N, N-Dimethylformamide (DMF, AR, 99.5%, Shanghai Aladdin Biochemical Technology Co.,Ltd) and acetone (AR, 99.5% Sinopharm Chemical Reagent Co.,Ltd), in which DMF/acetone volume ratio is 2:3. Second, 1g PVDF (solef 6010, Mw = 500,000 – 600,000 g/mol, Solvay S.A) was gradually added into the solution. Third, the mixture was magnetically stirred at 50°C for 5h to dissolve the polymer powders completely to get a homogeneous solution.

## 2.2 Electrospinning Deposition

During electro-spinning, the temperature and relative humidity were set as 27°C and 40~60%, respectively. Then, setting the injected rate to 1.0 mL/h with a 19-gauge stainless steel needle (inner diameter = 0.72 mm). The applied voltage and distance were respective 11.20 kV and 12 cm. A rotating metallic cylinder covered with an Al foil was used as the fiber collector in a rotating speed of 3000 rpm, and the spinning sprayers moved evenly with a speed of 2.6 mm/s. Finally, the highly oriented fiber membrane was obtained and then dried at 60°C overnight to ensure that the residual solvent evaporated completely.

## 2.3 Fabrication of the PZT/PVDF PENGs

The fiber films were fabricated by a laminating method as follows: cutting the fiber membrane into small pieces with the size 2 cm × 4 cm, adding them layer by layer along the same direction and then applying a press of 15MPa for one hour at 30 °C. Finally, all the fiber layers were compressed together and the fiber film with a certain thickness was fabricated. The nickel tape acting as electrodes was fixed tightly on the either surface of the fiber film. Further, thin PET films(30μm) were selected to package all the samples in case of pollution on the film surface when they were exposed to the lab environment. The samples with 0, 2 wt.%, 4 wt.%, 6 wt.%, 8 wt.% and 10 wt.% PZT content were respectively named as f-P 0.00, f-P 0.02, f-P 0.04, f-P 0.06, f-P 0.08 and f-P 0.10, in which f means fibers, P means PZT particles and 0.00-0.10 means the mass fraction of PZT particles.

**Fig. 1** The abridged general view of the PENGs process routing

## 2.4 Characterizations

The morphology of composite films was observed by the scanning electron microscopy (SEM, SU-8010, Hitachi, Japan). A mapping test was conducted on the PVDF/PZT fibers with the energy dispersive X-ray spectroscopy to characterize the elements and their distribution. Phase structures of the films were analyzed by X-ray diffraction (XRD, X'Pert PRO, PANalytical, Netherlands) with Cu/K $\alpha$  radiation. Besides, to explore the crystalline phase of PVDF in more detail, differential scanning calorimetry analysis (DSC,

Q200, TA Instruments, America) and Fourier-transform infrared spectroscopy (FTIR, Nicolet 5700, Thermo Fisher, America) were used. The surface characteristics were tested by Analysis IR2 (nanoIR2-fs, Analysis Instruments, America). The output voltages of PZT/PVDF fiber-based PENGs were collected by a digital oscilloscope (TBS2104, Tektronix, America). The output currents were calculated based on Ohm's law:  $I = U/R$  ( $I$ ,  $U$  and  $R$  respectively represent current, voltage and resistance.) through loading external resistance. The mechanical performance of the films was analyzed at room temperature by the tension test (Zwick/Roell Z020, Germany).

## Results And Discussion

### 3.1 Fibers Morphology and Device Structure

As a method for preparing nano/micro-scale composite fibers, electrospinning has been widely applied in the field of energy harvesting. From this work, we successfully prepared PVDF oriented fibers doped with PZT particles by adjusting the parameters of electrospinning and the viscosity of the mixed solution. In Fig. 2(a), the PZT/PVDF fibers show a high degree of orientation. Theoretically, aligned fibers are easier to be compressed than disordered ones without the obstruction of cross fibers. Moreover, the aligned fiber membranes show higher piezoelectric output performance than the disordered fibers membranes owing to uniformly oriented direction of  $\beta$  phase [28]. The element mapping of Zr, Ti, Pb and O are respectively displayed in Fig. 2(a<sub>1</sub>-a<sub>4</sub>), each element is evenly distributed over the fibers regardless of the particle sizes. It is worth noting that the PZT particles in the experiment are irregular blocks (Fig. S1(a)) which possess larger specific surface area and provide more space for the formation of polar phases than spherical PZT particles. The PZT particle size statistics and the XRD result are exhibited in Fig. S1(b) and Fig. S1(c). The fibers diameter distribution (Fig. 1(b)) in accordance with Fig. 1(a) ranges from 0.5 $\mu$ m to 3.0 $\mu$ m. Actually, when PZT content increases, the mixed solution becomes more viscous and thus the average fiber diameter becomes larger, which is shown in Fig. S2.

Owing to the loose structure of the fiber membranes, the output signal is weak and unstable that it is susceptible to surroundings. To solve the problem, a laminating method is used to compress several fiber membranes together[29]. It is worth noting that we conduct the process at room temperature (30°C) to minimize the impact of temperature on the porous structure. Herein, we superimpose the membranes layer by layer (2, 4, 6, 8 and 12 layers, respectively), and then compressed them under 15MPa for 60 minutes. The fiber films with thicknesses of ~40 $\mu$ m, ~100 $\mu$ m, ~160 $\mu$ m, ~190 $\mu$ m, ~220 $\mu$ m were obtained. As shown in Fig. 3(a), the 240 $\mu$ m film remains good flexibility. As the schematic structure shows (Fig. 3(b)), the PENG is composed of PENG packing layers, nickel tape layers, surface fibers and layers of internal fibers. The cross-section of the fiber film in Fig. 3(c) shows no obvious interface, indicating that layers of fiber membranes were well pressed together under the laminating treatment. Different from traditional laminate materials, the surface fibers (Fig. 3(d)) were squeezed together, which enhanced the density of fibers on the surface. While the internal fibers (Fig. 3(e)) still separated from each other, remaining porous inside. This structure not only increases the bound charge density on the surface to optimize piezoelectric output, but effectively improves the sensitivity of the composites. Besides, the inset

of Fig. 3(e) is the zoom-in view of one single fiber and the typically pillar wrinkled surface is generally helpful to piezoelectric outputs[30].

Based on the morphology of fibers, we studied the mechanical properties of the  $\sim 220\ \mu\text{m}$  f-P 0.10 film, as well as the 10wt.% PZT/PVDF cast film( $220\ \mu\text{m}$ ). The tensile test was performed at a drawing speed of 2 mm/min, and the strain curves in Fig. 3(f) exhibit a significant difference among the cast film and the fiber film under the conditions that the tensile is perpendicular/parallel to the axial direction of the fibers. In comparison with the cast film, the Young's modulus of fiber film dropped sharply from 1614 MPa to 499.2 MPa (F// fibers) and 227.2 MPa (F $\perp$  fibers), indicating that the fiber film is more flexible; The elongation at break of the fiber film increased to 262.3%, 14.8 times the breakage elongation of the cast film, which means that the fiber film has better toughness. (Fig. 3(g)) Although the maximum tensile strength is reduced to 8.538 MPa, it has little impact on the fiber film because it is mainly subjected to pressure rather than tension during application. The decrease in Young's modulus and tensile strength may be attributed to the lower crystallinity of the fiber film, which will be mentioned in the following paragraphs. At the same time, more amorphous regions lead to an increase in elongation at break. Table S1 lists the average Young's modulus, maximum tensile strength and elongation at break of f-P 0.10 film at different stretching directions and the 10wt.% PZT/PVDF cast film.

### 3.2 Crystalline Structure

In Fig. 4(a), the XRD results of the PVDF cast/fiber films with different PZT mass ratios exhibit the characteristic peaks of both PVDF and PZT. The typical peaks of perovskite PZT phase[31] are detected in all PZT/PVDF composite films, and the intensity gradually enhanced as PZT content increases. The enlarged view of XRD patterns from  $15^\circ$  to  $25^\circ$  is illustrated in Fig. 4(b), the pure cast film presented prominent peaks at  $2\theta=18.8^\circ$  and  $2\theta=20.2^\circ$ , respectively corresponding to the (020) and (110) reflections of  $\alpha$  phase. For fiber films, the peak at  $2\theta=18.8^\circ$  disappears and the peak at  $2\theta=20.2^\circ$  shifts to higher degree of  $2\theta=20.6^\circ$ , which corresponds to the (110) reflection of polar  $\beta$  phase. This phenomenon is attributed to high electric poling and mechanical stretching during electrospinning process. The applied electric field and stretching generally have a positive effect on the transformation of amorphous phase to polar  $\beta$  phase[30]. In Fig. 4(c), the curves become smoother as PZT concentration increases. For PZT particles, the excellent ferroelectricity makes them easier to be polarized by the applied electric field and the large remnant polarization avails better piezoelectricity. PZT particles also boost the formation of  $\beta$  phase. Specifically, charges on the polarized PZT particle surface affects the arrangement of PVDF molecules. The interaction between the positive/negative charges on PZT surface and the electronegative  $-\text{CF}_2$ /electropositive  $-\text{CH}_2$  groups on PVDF facilitates alignment of PVDF chains and promotes the formation of  $\beta$  phase[26,32]. In addition, it is believed that metal oxides carry hydroxyl groups on their surface. The attraction between the hydroxyl groups ( $-\text{OH}$ ) on PZT particles and the  $-\text{CF}_2$  groups of the PVDF polymer chains results in the generation of  $\beta$  phase, which also supports the experimental results.

To further study the structure and crystalline characteristics of the composite fiber film, the FTIR spectra in ATR mode and DSC measurement were performed. In Fig. 4(d), the pure PVDF cast film contains

several typical characteristics absorption bands. The peak at 764 cm<sup>-1</sup> is designated as  $\alpha$  phase[33]; The peaks of  $\gamma$  phase are located at 812 cm<sup>-1</sup> [34,35], 834 cm<sup>-1</sup> [36]and 1234 cm<sup>-1</sup> [37]. The polar  $\beta$  phase comes from the absorption bands of 1074 cm<sup>-1</sup> and 1430 cm<sup>-1</sup>[38]. For the fiber film, two new peaks corresponding to  $\beta$  phase appear at 840 cm<sup>-1</sup> and 1275 cm<sup>-1</sup>. Besides, the  $\beta$  phase at 1430 cm<sup>-1</sup> is enhanced, while  $\alpha/\gamma$  phase reduces. The incorporation of PZT particles further suppressed the intensity of  $\alpha$  and  $\gamma$  phases. The observed result of FTIR spectra is consistent with the XRD data and the amount of  $\beta$  phase is calculated, the equation[39] is:

$$F_{\beta} = \frac{I_{\beta}}{(k_{\beta}/k_{\alpha}) \times I_{\alpha} + I_{\beta}} \quad (1)$$

Where,  $I_{\alpha}$  refers to the absorbance of  $\alpha$  phase at 764cm<sup>-1</sup> in the FTIR spectrum;  $I_{\beta}$  is the absorbance of  $\beta$  phase at 840cm<sup>-1</sup> in the FTIR spectrum;  $K_{\alpha}$  and  $K_{\beta}$  are constants and represent absorption coefficients. The calculation results are shown graphically in Fig. 4(f), the data shows electrospinning process does enhance the percentage of  $\beta$  phase, but it is not as much as we expected. The f-P 0.00 film have 76.31%  $\beta$  phase, which is lightly higher than the cast film (76.13%). Interestingly, the addition of PZT particles significantly promoted  $\beta$  phase content, reaching a maximum of 83.16% in the f-P 0.04 film. When the PZT particles content further increases, the resultant viscosity increases to causes difficulties in the mixed solution ejecting out of the needle tip even at a higher electric field application. As a result, there is a tendency of the resultant dispersion to form higher diameter fibers with less effective orientation of the polymer chains which emphasizes the growth of an  $\alpha$  phase rather than  $\beta$  phase[40]. Such phenomena can also be reflected in the crystallization curves (Fig. 4(e)) of the fiber composites and the overall crystallization was calculated using the formula:

$$\chi_c = \frac{\Delta H_f}{(1-\phi) \times \Delta H_m^{100}} \quad (2)$$

Where,  $\chi_c$  represents the degree of crystallinity,  $\Delta H_f$  is melting enthalpy of PVDF/PZT composites,  $\phi$  is mass ratio of PZT particles in PVDF/PZT composite and  $\Delta H_m^{100}$  represents the melting enthalpy of a 100% crystalline PVDF( $\Delta H_m^{100} = 104.7$  J/g). In Fig. 4(f), the crystallinity of the f-P 0.00 film is 50.16%, slightly lower than that of the cast film (50.35%). Too many interfaces between the fibers reduce the chance of crystallization. PZT particles significantly improves the crystallinity of the fiber film, which owes to the increase of  $\beta$  phase when PZT content is 2%-4% and the formation of  $\alpha$  phase when the PZT content is 6%-10% because the higher diameter fibers with less effective polymer chains stretching favor the generation of  $\alpha$  phase instead of  $\beta$  phase.

### 3.3 Surface Characteristics

Essentially, the piezoelectric performance depends on the polarization intensity brought about by the internal crystal structure, and also depends on the bound charge density of the film surface. Here, we

studied the characteristics of the internal/surface fibers of f-P 0.10 film(220 $\mu$ m) and 10wt.% PZT/PVDF cast film(220 $\mu$ m) for comparison. Firstly, the topographic maps are shown in Fig. 5(a-c). The surface of the cast film is flat, which is concluded from that the overall color is almost indistinguishable in Fig. 5(a). Internal fibers in Fig. 5(b) show rougher surfaces with a wider range of colors than surface fibers in Fig. 5(c), verifying that the laminating process improves the density and flatness of the surface fibers without destroying the porous fibrous structure. Secondly, the surface potential positively correlated with the surface charge density is showed in Fig. 5(d-f). In contrast to the cast film, both surface fibers and internal fibers exhibit stronger potentials with the color shifting to red or blue. Whether it is positive or negative rests with the testing surface as overall polarization intensity is parallel to the thickness direction and directional. This is a pretty good proof that multi-layered porous fiber film has more surface charges than the cast film. Thirdly, the surface phases are also discussed in Fig. 5(g-i). To ensure that the color distinction shown in 2-D image is attributed to the reflection of different phases, not the surface height gap, the 3-D images have also been displayed in Fig. 5(j-l). Obviously, 2-D and 3-D do not share the same pattern. Despite it is impossible to distinguish each specific color corresponding to a specific phase, there is a striking contrast between the fiber film and cast film, especially in 3-D images. The surface phases image of the cast film shown in Fig. 5(j) looks like green grass, and shows greater stiffness in accordance with the results of the tensile test, which proves greater crystallinity. It may be mainly composed of nonpolar  $\alpha$  phase and amorphous polymer. While the surface phases image of fibers in Fig. 5(k) and Fig. 5(l) looks more like a yellow forest, where more polar  $\beta$  phase, less  $\alpha$  phase and more amorphous polymer exist. The orange regions indicate the gaps between the fibers or the holes on fibers. It is worth mentioning that there is almost no difference in surface potential and phases between surface and internal fibers, suggesting that mechanical compression makes no difference to the crystalline structure of the PZT/PVDF composite fibers[41].

### 3.4 Piezoelectric Properties

Fig. 6(a) illustrates a piezoelectric model of the PZT/PVDF fiber-based PENGs. Here, the  $-\text{CH}_2\text{-CF}_2-$  chains in PVDF and the polarized ferroelectric domains in PZT particles are regarded as dipoles, as shown in Fig. 6(b). Under the high-potential electric field in the electrospinning process, most of dipoles rotate to the same direction, generating an internal electric potential inside the film. To balance the potential, external electrons are bound to the surface. When external pressure is applied, the PENG is compressed by and the dipoles rotate, reducing the internal dipolar momentum along the film thickness. At the same time, the bound electrons on the surface show an opposing potential and the film exhibits polarity as a whole. As becomes longer, the overall polarization increases, followed by an increase in output voltage (Fig. 6(a-ii)). The free electrons in electrodes gradually flow to the high-potential side through external circuit to offset the potential difference. When the compression deformation reaches , the film reaches a new balance and shows no polarity. At this time, the output voltage drops to zero. Subsequently, when the external pressure is released, dipoles rotate to the original state gradually, thereby generating a reverse output voltage and the free electrons flow back to the original side.

Considering that the frequency of driving pressure from human motion (walking, running, joint motions, etc) is relatively low, the output voltage signals were collected at a frequency of 3 Hz under a periodic pressure of 5 N. Since PZT has a large piezoelectric constant, it is speculated that PZT particles play a predominant role in the piezoelectric performance of the composite[28,36]. The more incorporation of PZT particles, the better electrical output performance of the PENGs. However, when PZT content exceeds 10 wt.%, the consequent viscosity increase creates difficulties in the ejection of the composite solution out of the needle tip. Therefore, we first explored the output voltage of f-P 0.10 fiber-based PENGs with thicknesses of  $\sim 40\mu\text{m}$ ,  $\sim 100\mu\text{m}$ ,  $\sim 160\mu\text{m}$ ,  $\sim 190\mu\text{m}$ ,  $\sim 220\mu\text{m}$ . As shown in Fig. 7(a), all signals are very stable and the voltage peak tends to rise as the film thickness increases. The laminating process increased dipolar momentum and overall polarization inside the film, followed by the improvement of piezoelectric conversion capacity. In addition, it is expected that the capacity can be further enhanced by increasing thickness. For example, when the thickness is  $500\mu\text{m}$ , the output voltage can reach as high as 92V (Fig. S3). Secondly, at the same thickness of  $\sim 220\mu\text{m}$ , we studied the output voltage of the fiber-based PENGs with the PZT content of 0, 2wt.%, 4wt.%, 6wt.%, 8wt.% and 10 wt.%. In Fig. 7(b), the output voltage is positively correlated with the content of PZT particles, and reaches maximum of 62.0 V in the sample f-P 0.10 fiber-based PENG. It is about 8.3 times the output voltage of the f-P 0.00 fiber-based PENG (7.5 V) because PZT particles not only possess strong piezoelectricity, but also promote polar  $\beta$  phase generating in PVDF. To prove the superiority of the fiber-based PENGs, cast film-based PENGs with the same film thickness were prepared as a comparison. In Fig. 7(c), the f-P 0.10 fiber-based PENGs output 3.7 times ( $100\mu\text{m}$ ) and 3.4 times ( $220\mu\text{m}$ ) the voltage of the 10 wt.% PZT/PVDF cast film-based PENGs, respectively. Further, The PENG with a film thickness of  $220\mu\text{m}$  was connected to different load resistances ranging from  $1\text{ M}\Omega$  to  $800\text{ M}\Omega$  (Fig. 7(d)). As the load resistance increases to  $500\text{ M}\Omega$ , the load voltage gradually rises to a constant value  $\sim 83\text{ V}$ , whereas the load current gradually decreases from  $7.6\mu\text{A}$  to  $0.105\mu\text{A}$ . Correspondingly, the maximum output power is  $136.9\mu\text{W}$  at the load resistance of  $10\text{ M}\Omega$ , which is 6.5 times the power of the  $220\mu\text{m}$  thick cast film-based PENG ( $21.025\mu\text{W}$ ) (Fig. 7(e)).

For verifying the piezoelectric signal, a switching polarity test was carried out[37,42]. As Fig. 7(f) shows, the output voltage reverses as the circuit connection reverses, confirming that the signals are authentic piezoelectric outputs. The output performance stability was also tested under compressing and bending modes. As seen in Fig. 7(g) and Fig. 7(h), the output voltage of the f-P 0.10 fiber-based PENG is stable after 3000 circles. Benefit from the multi-layered porous structure, the f-P 0.10 fiber-based PENG ( $220\mu\text{m}$ ) shows high sensitivity to pressure. Under the pressure of  $\sim 2\text{ N}$ , its output voltage reaches  $\sim 20\text{V}$ . Sensitivity is also a parameter for evaluating piezoelectric output performance, and its expression[43] is:

$$S = \frac{U}{F} \quad (3)$$

Where,  $S$  is the sensitivity,  $U$  is the output voltage, and  $F$  represents the applied pressure. The calculated sensitivity of the fiber-based PENG is  $12.4\text{ V N}^{-1}$ , which is 3.4 times the sensitivity of the cast film-based PENG ( $3.6\text{ V N}^{-1}$ ). It is superior to most reported PENGs with porous structure, and the comparison is listed in Table 2.

**Table 2** Comparison of output performance with different porous structures

Piezoelectric filler	Matrix	Structure	Voc(V)	Stress	Sensitivity	Ref.
BT NP	PVDF	Oriented	150	100 N	$1.5 \text{ VN}^{-1}$	44
BCZTY NW	PDMS	Electrospun-oriented	3	Finger-Taping	–	21
BT NP	PDMS	Porous-interconnected	15.5	32 N	$0.48 \text{ VN}^{-1}$	14
BFO NP	PDMS	3-D interconnected	16	35 N	$0.46 \text{ VN}^{-1}$	12
Sm-PMN-PT NP	PDMS	Porous-interconnected	60	35 N	$1.71 \text{ VN}^{-1}$	10
PZT NP	PDMS	Gradient-porous	152	100 N	$1.52 \text{ VN}^{-1}$	43
PZT P	PVDF	Electrospun-oriented	62	5 N	$12.4 \text{ VN}^{-1}$	This work

Further application potential of the f-P 0.10 fiber-based PENG (220  $\mu\text{m}$ ) has been investigated, in which a rectifier bridge is used to convert AC output to DC output (Fig. 8(a)). Fig. 8(b) shows the rectified voltage signal of  $\sim 58 \text{ V}$ , which directly lights up 21 LED lights in series. We also charged the capacitors with the capacitances of 1  $\mu\text{F}$ , 3.3  $\mu\text{F}$ , 10  $\mu\text{F}$ , 22  $\mu\text{F}$  and 47  $\mu\text{F}$ . As shown in Fig. 8(c), the capacitor (1  $\mu\text{F}$ ) voltage rapidly increases to 6.4 V within 65 s and remains stable, which means that the charging voltage tends to be a constant value at 6.4 V. The others got to 3.53 V, 1.03 V, 0.82 V and 0.20 V, respectively. Besides, the curves increase proportionally, showing further potential for reaching the maximum charging voltage. Further, to simulate the applied scenarios, some simple human actions were applied in energy harvesting, such as finger pressing, fist beating, one side bending, and pressing on the arm. As Fig. 8(e-h) shows, the corresponding output voltage reaches  $\sim 20 \text{ V}$ ,  $\sim 30 \text{ V}$ ,  $\sim 18 \text{ V}$ , and  $\sim 4 \text{ V}$ , respectively, clarifying that the PENGs are the promising devices to harvest mechanical energy from human motions.

## Conclusion

Porous, multi-layered PZT/PVDF piezoelectric fiber composites composed of contact surface fibers and separated internal fibers were fabricated by laminating process. PENGs based on the porous fibrous PZT/PVDF composites with various thickness and PZT content for harvesting mechanical energy have also been developed. The laminated fiber film not only has a strong internal polarization to achieve excellent piezoelectric output, but also has a porous structure to ensure piezoelectric sensitivity. Therefore, the PENG based on the 10wt.% PZT/PVDF fiber film ( $\sim 220 \mu\text{m}$ ) output the maximum power of 136.9  $\mu\text{W}$ , almost 6.5 times the power of the 10 wt.% PZT/PVDF cast film-based PENG (21.025  $\mu\text{W}$ ). Its sensitivity is  $12.4 \text{ VN}^{-1}$ , which is superior to most reported PENGs with porous structures. Further, the corresponding output voltage of 62V was applied in capacitor charging and LEDs lighting, in which the

capacitor (1  $\mu\text{F}$ ) was charged rapidly to 6.3 V within 65s and 21 commercial green LEDs were driven to illuminate directly. The porous, multi-layered PZT/PVDF composite fibers present an effective advancement in sensors, energy harvesting and low-power electric devices with the requirement of self-powered characteristics.

## Declarations

## Acknowledgement

The authors gratefully acknowledge the financial support from the National Natural Science Foundation of China (Grant No. 51772267) and the Key R&D Program of Zhejiang Province (Grant No. 2020C01004)

## References

1. Huan Y, Zhang X, Song J et al (2018) High-performance piezoelectric composite nanogenerator based on Ag/(K, Na)NbO<sub>3</sub> heterostructure. *Nano Energy* 50:62–69
2. Zhang MH, Hu C, Zhou Z et al (2020) Determination of polarization states in (K,Na)NbO<sub>3</sub> lead-free piezoelectric crystal. *J Adv Ceram* 9(2):204–209
3. Shi K, Sun B, Huang X et al (2018) Synergistic effect of graphene nanosheet and BaTiO<sub>3</sub> nanoparticles on performance enhancement of electrospun PVDF nanofiber mat for flexible piezoelectric nanogenerators. *Nano Energy* 52:153–162
4. Okayasu M, Ogawa T (2019) Effects of loading contact on electric-power generation of lead zirconate titanate piezoelectric ceramic plate. *J Adv Ceram* 8(4):509–518
5. Bobić JD, Teixeira GF, Grigalaitis R et al (2019) PZT–NZF/CF ferrite flexible thick films: Structural, dielectric, ferroelectric, and magnetic characterization. *J Adv Ceram* 8(4):545–554
6. Lu MY, Song J, Lu MP et al (2009) ZnO – ZnS heterojunction and ZnS nanowire arrays for electricity generation. *ACS Nano* 3(2):357–362
7. Wang ZL, Song J (2006) Piezoelectric nanogenerators based on zinc oxide nanowire arrays. *Science* 312(5771):242–246
8. Lin YF, Song J, Ding Y et al (2008) Alternating the output of a CdS nanowire nanogenerator by a white-light-stimulated optoelectronic effect. *Adv Mater* 20(16):3127–3130
9. Zhang Y, Jeong CK, Wang J et al (2018) Flexible energy harvesting polymer composites based on biofibril-templated 3-dimensional interconnected piezoceramics. *Nano Energy* 50:35–42
10. Zhang C, Fan Y, Li H et al (2018) Fully rollable lead-free poly (vinylidene fluoride)-niobate-based nanogenerator with ultra-flexible nano-network electrodes. *ACS Nano* 12(5):4803–4811
11. Zhang Y, Wu M, Zhu Q et al (2019) Performance enhancement of flexible piezoelectric nanogenerator via doping and rational 3D structure design for self-powered mechanosensational system. *Adv Funct Mater* 29(42):1904259

12. Koka A, Sodano HA (2013) High-sensitivity accelerometer composed of ultra-long vertically aligned barium titanate nanowire arrays. *Nat Commun* 4(1):1–10
13. Shi K, Huang X, Sun B et al (2019) Cellulose/BaTiO<sub>3</sub> aerogel paper based flexible piezoelectric nanogenerators and the electric coupling with triboelectricity. *Nano Energy* 57:450–458
14. Zhang G, Zhao P, Zhang X et al (2018) Flexible three-dimensional interconnected piezoelectric ceramic foam based composites for highly efficient concurrent mechanical and thermal energy harvesting. *Energy Environ Sci* 11(8):2046–2056
15. Dong K, Peng X, Wang ZL (2020) Fiber/fabric-based piezoelectric and triboelectric nanogenerators for flexible/stretchable and wearable electronics and artificial intelligence. *Adv Mater* 32(5):1902549
16. Xie M, Hisano K, Zhu M et al (2019) Flexible multifunctional sensors for wearable and robotic applications. *Adv Mater Technol* 4(3):1800626
17. Xue J, Wu T, Dai Y et al (2019) Electrospinning and electrospun nanofibers: Methods, materials, and applications. *Chem Rev* 119(8):5298–5415
18. Cozza ES, Monticelli O, Marsano E et al (2013) On the electrospinning of PVDF: influence of the experimental conditions on the nanofiber properties. *Polym Int* 62(1):41–48
19. Wu Y, Ma F, Qu J et al (2019) Vertically-aligned lead-free BCTZY nanofibers with enhanced electrical properties for flexible piezoelectric nanogenerators. *Appl Surf Sci* 469:283–291
20. Kim SR, Yoo JH, Kim JH et al (2021) Mechanical and piezoelectric properties of surface modified (Na,K)NbO<sub>3</sub>-based nanoparticle-embedded piezoelectric polymer composite nanofibers for flexible piezoelectric nanogenerators. *Nano Energy* 79:105445
21. Chamankar N, Khajavi R, Yousefi AA et al (2020) A flexible piezoelectric pressure sensor based on PVDF nanocomposite fibers doped with PZT particles for energy harvesting applications. *Ceram Int* 46(12):19669–19681
22. Chamankar N, Khajavi R, Yousefi AA et al (2020) An experimental model for predicting the piezo and dielectric constant of PVDF-PZT nanocomposite fibers with 0–3 and 1–3 connectivity. *Ceram Int* 46(15):23567–23581
23. Chang J, Shen Y, Chu X et al (2015) Large  $d_{33}$  and enhanced ferroelectric/dielectric properties of poly(vinylidene fluoride)-based composites filled with Pb(Zr<sub>0.52</sub>Ti<sub>0.48</sub>)O<sub>3</sub> nanofibers. *RSC Adv* 5(63):51302–51307
24. Yun JS, Park CK, Jeong YH et al (2016) The fabrication and characterization of piezoelectric PZT/PVDF electrospun nanofiber composites. *Nanomater Nanotechnol* 6:20
25. Collins G, Federici J, Imura Y et al (2012) Charge generation, charge transport, and residual charge in the electrospinning of polymers: A review of issues and complications. *J Appl Phys* 111(4):044701
26. Holmes-Siedle AG, Wilson PD, Verrall AP (1983) PVdF: An electronically-active polymer for industry. *Mater Des* 4(6):910–918
27. Kong LB, Zhu W, Tan OK (2000) Preparation and characterization of Pb(Zr<sub>0.52</sub>Ti<sub>0.48</sub>)O<sub>3</sub> ceramics from high-energy ball milling powders. *Mater Lett* 42(4):232–239

28. Zaarour B, Zhu L, Huang C et al (2019) Enhanced piezoelectric properties of randomly oriented and aligned electrospun PVDF fibers by regulating the surface morphology. *J Appl Polym Sci* 136(6):47049
29. Liao Y, Wang R, Tian M et al (2013) Fabrication of polyvinylidene fluoride (PVDF) nanofiber membranes by electro-spinning for direct contact membrane distillation. *J Membrane Sci* 425:30–39
30. Chinaglia DL, Gregório R Jr, Vollet DR (2012) Structural modifications in stretch-induced crystallization in PVDF films as measured by small-angle X-ray scattering. *J Appl Polym Sci* 125(1):527–535
31. Kwok CK, Desu SB (1993) Low temperature perovskite formation of lead zirconate titanate thin films by a seeding process. *J Mater Res* 8(2):339–344
32. Araújo MC, Costa CM, Lanceros-Méndez S (2014) Evaluation of dielectric models for ceramic/polymer composites: Effect of filler size and concentration. *J Non-Cryst Solids* 387:6–15
33. Salimi A, Yousefi AA (2003) Analysis method: FTIR studies of  $\beta$ -phase crystal formation in stretched PVDF films. *Polym Test* 22(6):699–704
34. Gregorio R, Capitaó RC (2000) Morphology and phase transition of high melt temperature crystallized poly (vinylidene fluoride). *J Mater Sci* 35(2):299–306
35. Boccaccio T, Bottino A, Capannelli G et al (2002) Characterization of PVDF membranes by vibrational spectroscopy. *J Membrane Sci* 210(2):315–329
36. Guo D, Chen X, Chu X et al (2013) In situ observation of the nanocrystal growth and their piezoelectric performance change in P(VDF-TrFE) films by hot stage piezoresponse force microscopy. *J Appl Phys* 113(18):187210
37. He S, Dong W, Guo Y et al (2019) Piezoelectric thin film on glass fiber fabric with structural hierarchy: An approach to high-performance, superflexible, cost-effective, and large-scale nanogenerators. *Nano Energy* 59:745–753
38. Yu H, Huang T, Lu M et al (2013) Enhanced power output of an electrospun PVDF/MWCNTs-based nanogenerator by tuning its conductivity. *Nanotechnology* 24(40):405401
39. Cai X, Lei T, Sun D et al (2017) A critical analysis of the  $\alpha$ ,  $\beta$  and  $\gamma$  phases in poly (vinylidene fluoride) using FTIR. *RSC Adv* 7(25):15382–15389
40. Bairagi S, Ali SW (2020) Investigating the role of carbon nanotubes (CNTs) in the piezoelectric performance of a PVDF/KNN-based electrospun nanogenerator. *Soft Matter* 16(20):4876–4886
41. Chen N, Hong L (2002) Surface phase morphology and composition of the casting films of PVDF–PVP blend. *Polymer* 43(4):1429–1436
42. Zhou Z, Zhang Z, Zhang Q et al (2019) Controllable Core–Shell BaTiO<sub>3</sub>@Carbon Nanoparticle-Enabled P (VDF-TrFE) Composites: A Cost-Effective Approach to High-Performance Piezoelectric Nanogenerators. *ACS Appl Mater Inter* 12(1):1567–1576
43. Liu H, Lin X, Zhang S et al (2020) Enhanced performance of piezoelectric composite nanogenerator based on gradient porous PZT ceramic structure for energy harvesting. *J Mater Chem A*

44. Zhao Y, Liao Q, Zhang G et al (2015) High output piezoelectric nanocomposite generators composed of oriented BaTiO<sub>3</sub> NPs@PVDF. Nano Energy 11:719–727

## Figures

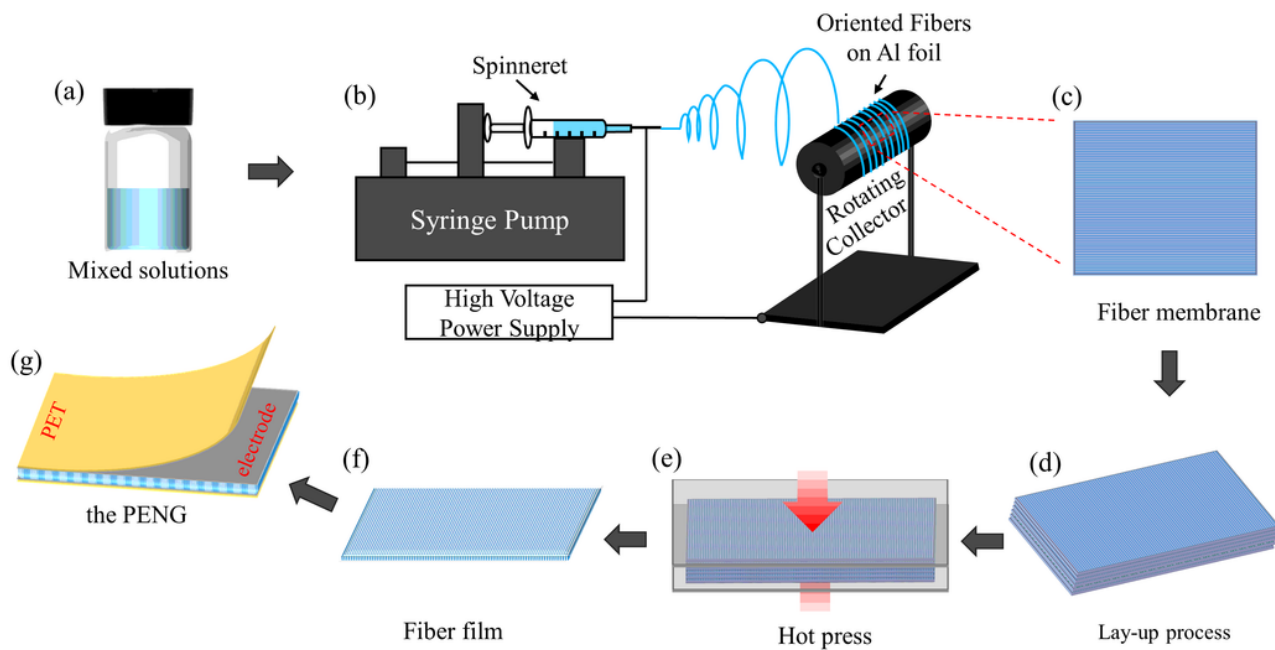
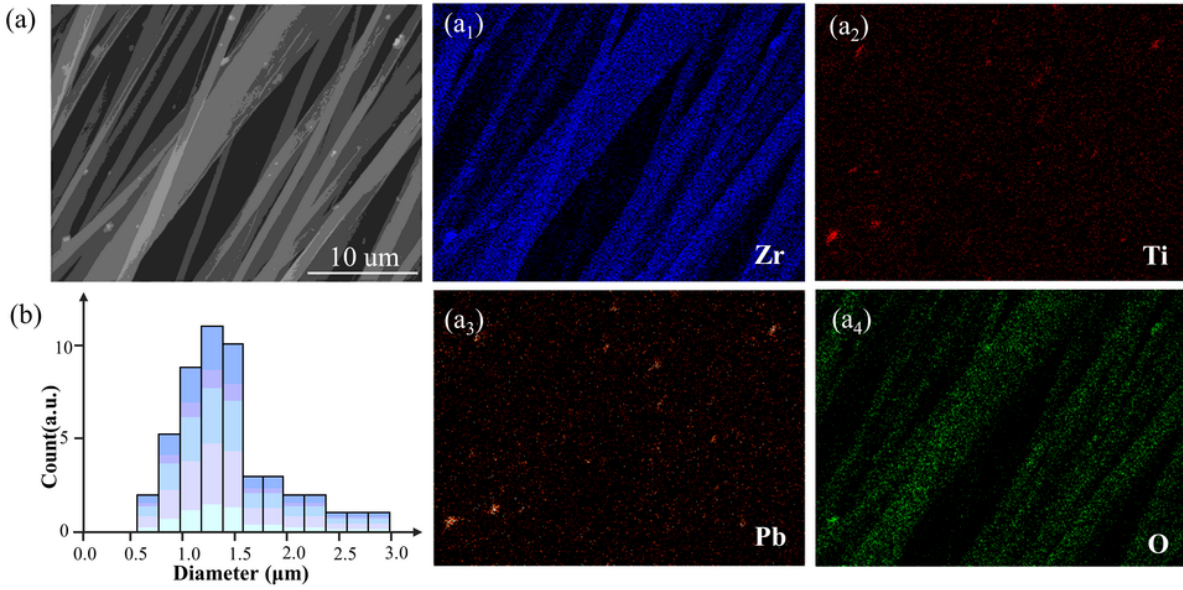


Figure 1

The abridged general view of the PENGs process routing



**Figure 2**

(a) SEM image of 10wt.% PZT/PVDF electrospinning fibers; (a1-a4) The element mapping of electrospinning fibers. (b) Statistical results of the fiber diameter distribution.

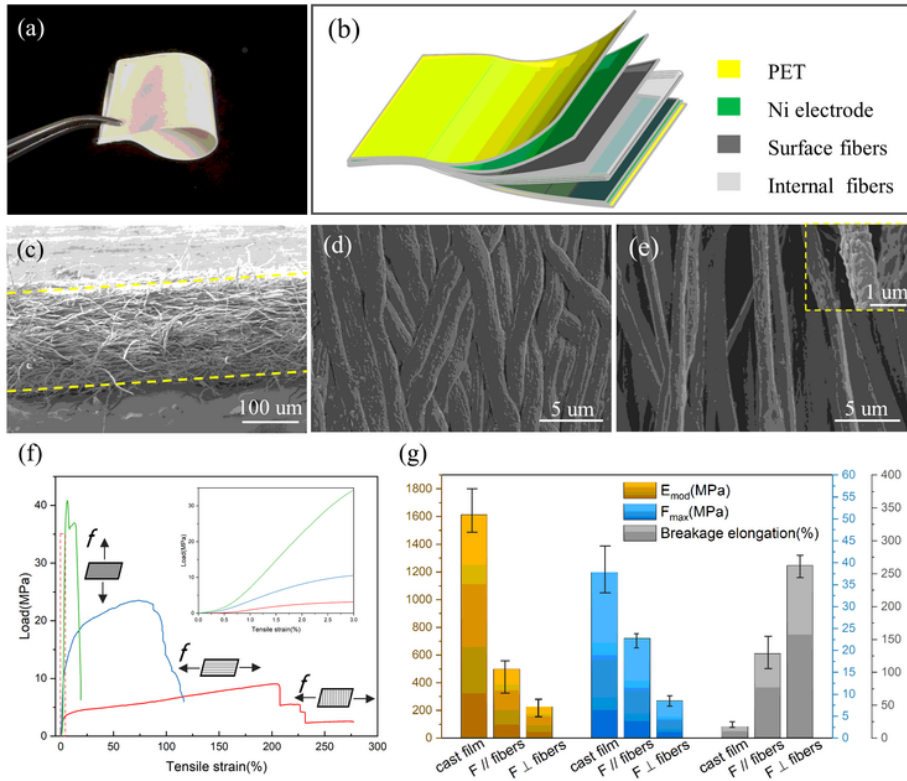


**Figure 3**

(a) Photograph of the fiber film; (b) Schematic structure of the PENGs; SEM image of (c) the fiber film cross section, (d) surface fibers and (e) internal fibers, inset: enlarged view of one single fiber; (f) the strain curves, (g) Young's modulus  $E_{mod}$ , maximum tensile strength  $F_{max}$  and breakage elongation of 10 wt.% PZT/PVDF film with a thickness of  $\sim 220 \mu\text{m}$ .

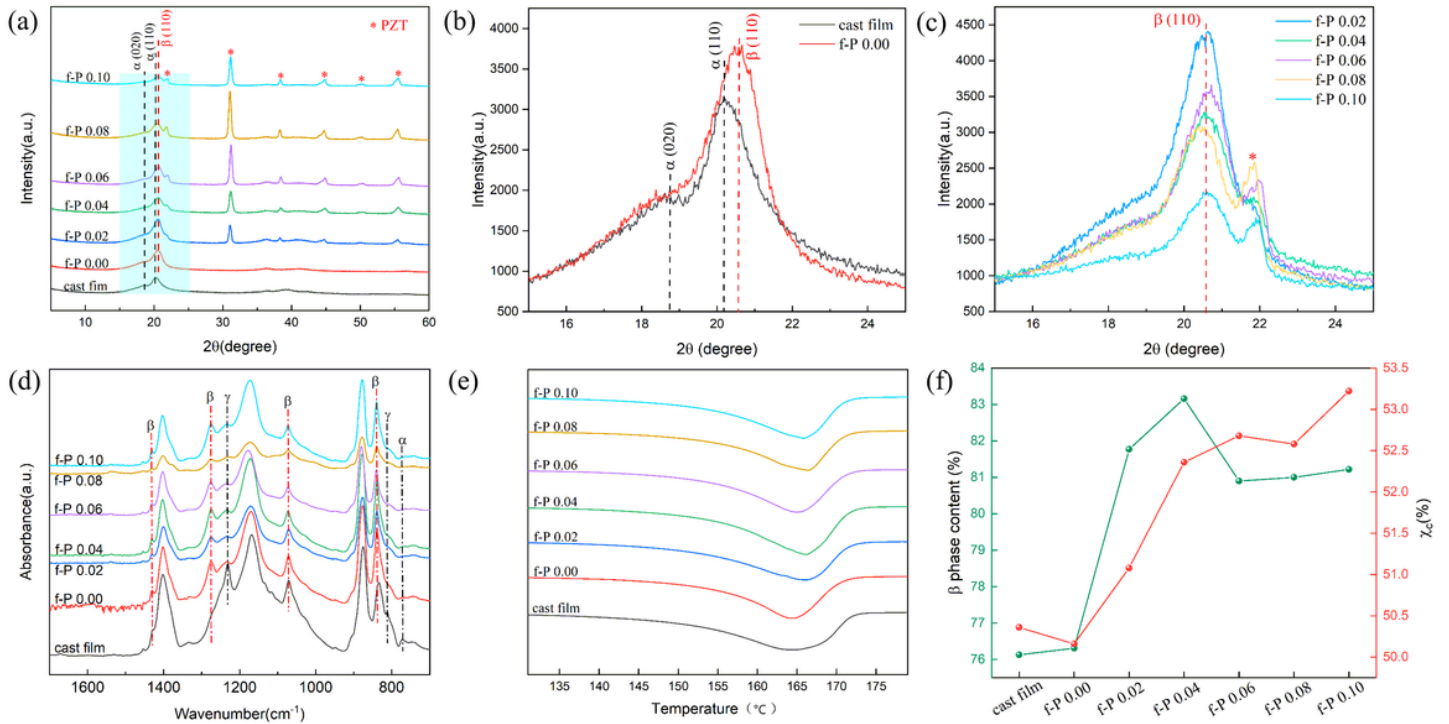


**Figure 4**

(a) The XRD patterns, (d) the FTIR spectra in ATR mode, (e) the DSC curves and (f) calculated crystallinity degree and  $\beta$  phase content of pure PVDF cast film and PZT/PVDF fiber films with different PZT concentrations; enlarged XRD view of (b) PVDF cast film and PVDF fiber film and (c) PZT/PVDF composite fiber films from 15 degree to 25 degree.

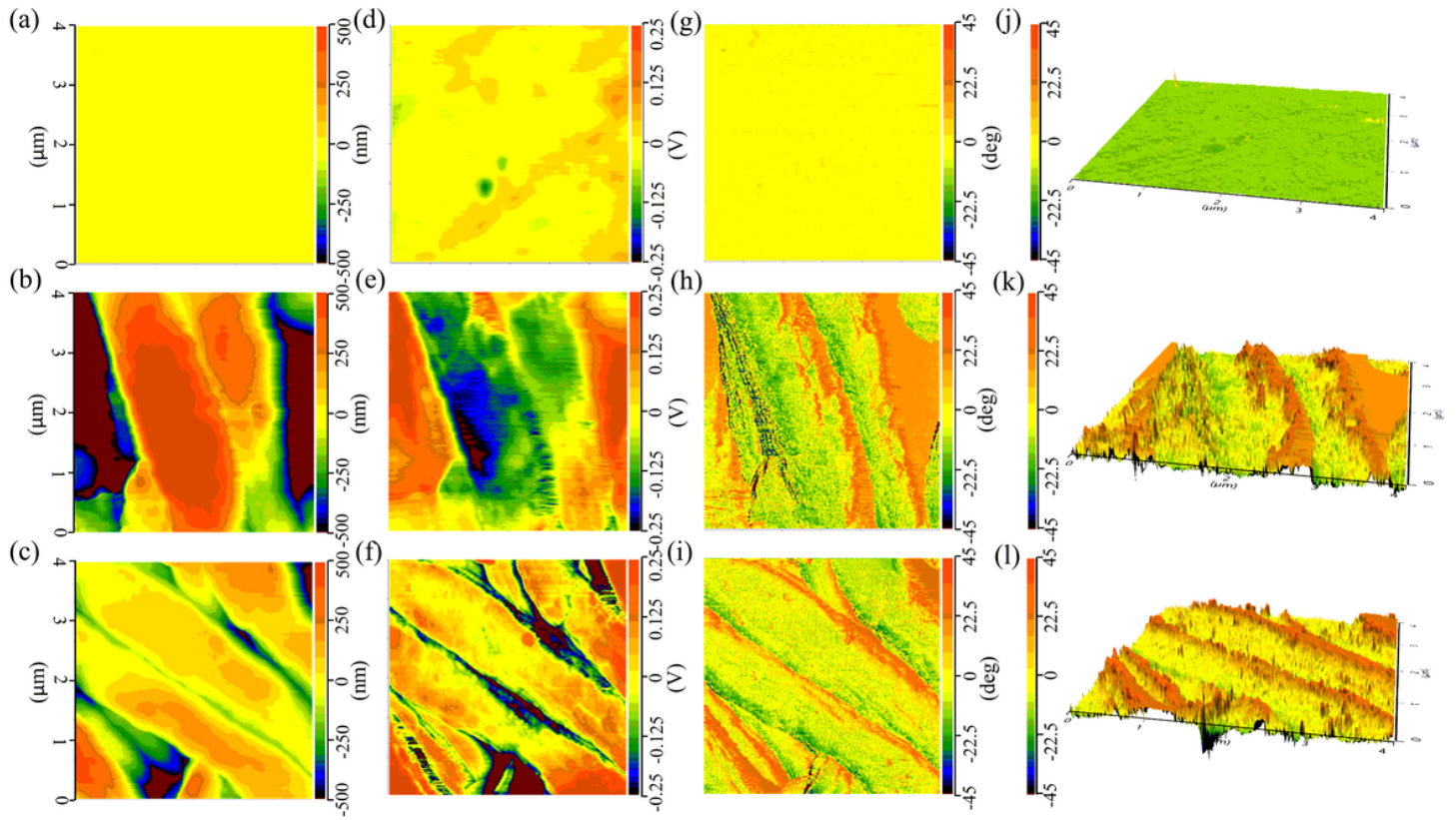


**Figure 5**

Topographic images of (a) cast film; (b) internal fibers; (c) surface fibers; KPFM images of (d) cast film; (e) internal fibers; (f) surface fibers; Phase images of (g)(j) cast film; (h)(k) internal fibers; (i)(l) surface fibers in 10wt.% PZT/PVDF PENGs.

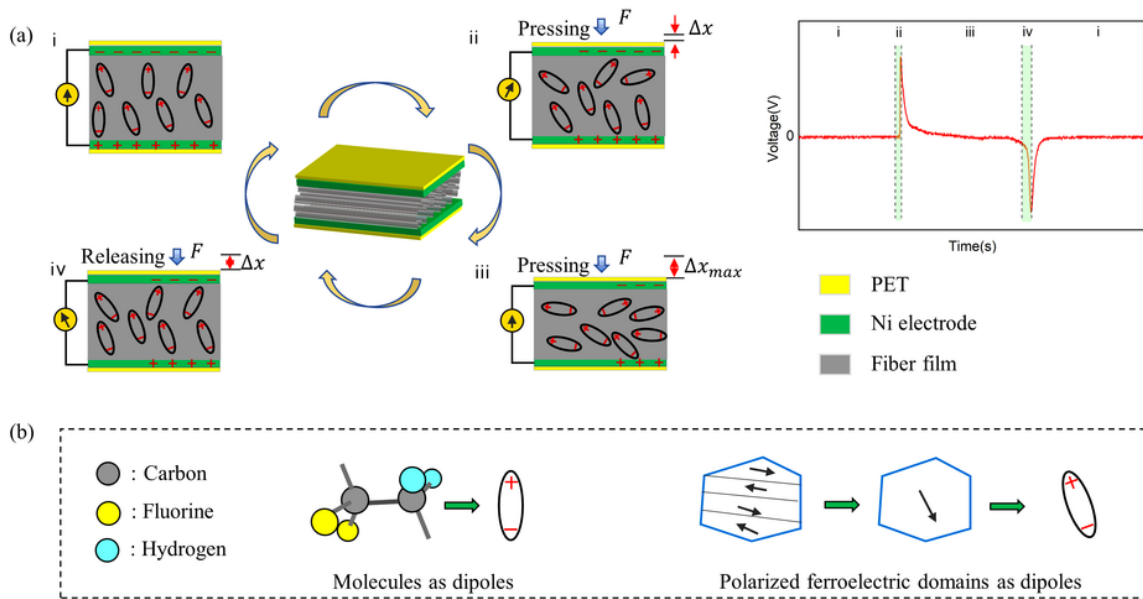


**Figure 6**

(a) Schematic diagram of the mechanism of the piezoelectric performance of PZT/PVDF fiber-based PENGs; (b) Abstract diagram of the dipoles about PVDF molecules and PZT ferroelectric domains inside the fibers.

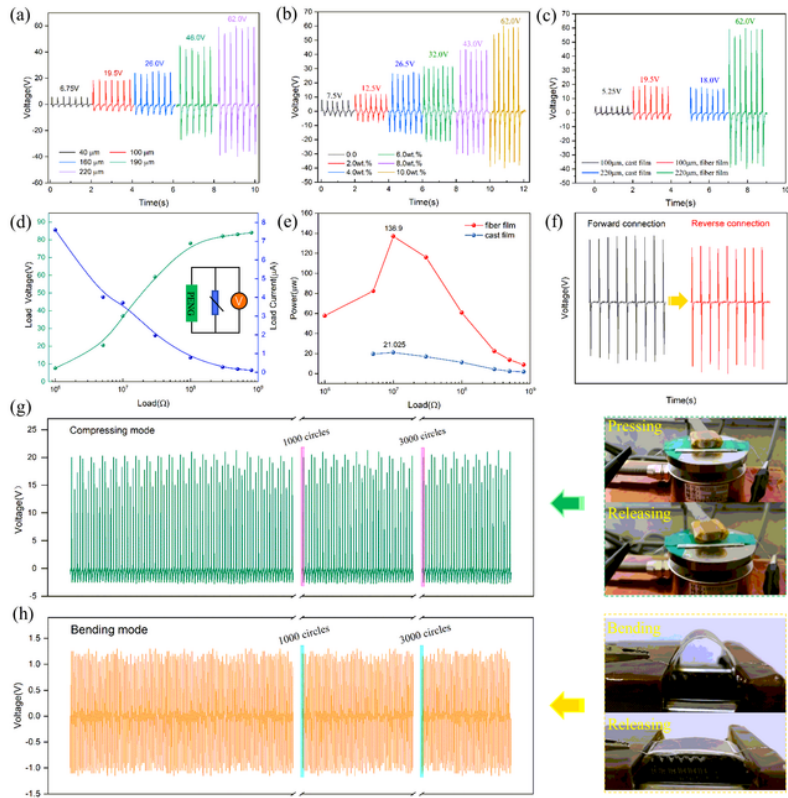


**Figure 7**

(a) Output voltage of f-P 0.10 fiber-based PENGs with different film thickness; (b) output voltage of fiber-based PENGs with various PZT content ( $\sim 220\mu\text{m}$ ); (c) output voltage contrast between the f-P 0.10 fiber-based PENGs and 10wt.% PZT/PVDF cast film-based PENGs; (d) output voltage and calculated currents, (e) output power of the f-P 0.10 fiber-based PENG with a film thickness of  $220\mu\text{m}$  under various external resistances load; (f) output voltage of f-P 0.10 fiber-based PENG in a condition of reversing electrodes; (g) cyclic output voltage of the f-P 0.10 fiber-based PENG ( $220\mu\text{m}$ ) under compressing mode with  $\sim 1.0\text{ N}$  pressure at a frequency of  $10\text{ Hz}$ . (h) cyclic output voltage of the f-P 0.10 fiber-based PENG ( $220\mu\text{m}$ ) under bending mode at a frequency of  $3\text{ Hz}$ .

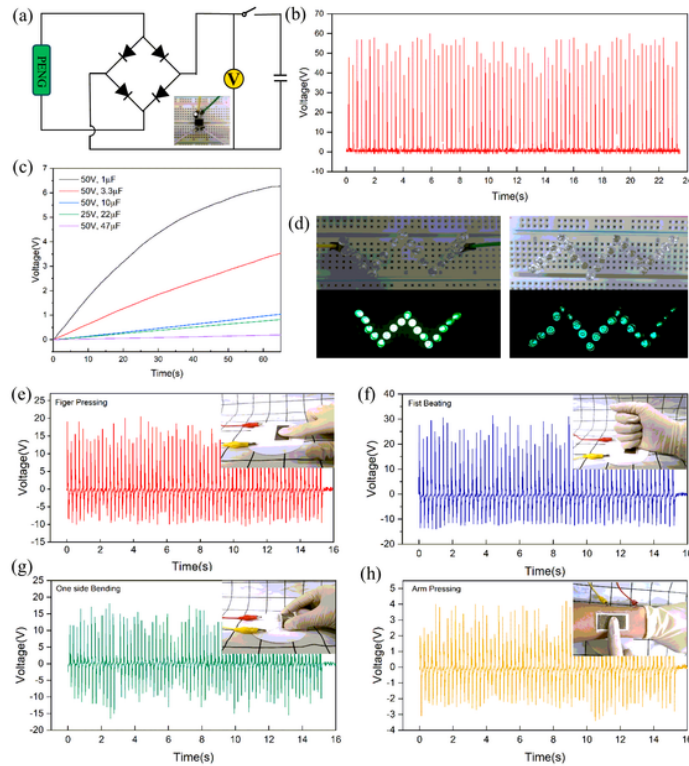


**Figure 8**

(a) Equivalent circuit diagram of the charging commercial capacitor with a charging system inset; (b) rectified voltage of f-P 0.10 fiber-based PENG with a thickness of  $\sim 220\mu\text{m}$ ; (c) charging voltages of various capacitors; (d) green LEDs lit by the rectified voltage of the PENG; Output voltage from f-P 0.00 fiber-based PENG under (e) finger pressing; (f) fist beating; (g) one side bending; (h) pressing on the arm.

## Supplementary Files

This is a list of supplementary files associated with this preprint. Click to download.

- [Supportinginformation.docx](#)